Monthly Notices of the ROYAL ASTRONOMICAL SOCIETY

MNRAS **517,** 1958–1969 (2022) https://doi.org/10.1093/mnras/stac2020
Advance Access publication 2022 July 23

Predictions for the X-ray circumgalactic medium of edge-on discs and spheroids

Anna Nica,[1,2] Benjamin D. Oppenheimer ,[1]★ Robert A. Crain ,[3] Ákos Bogdán,[4] Jonathan J. Davies ,[5] William R. Forman,[4] Ralph P. Kraft[4] and John A. ZuHone[4]

[1]*CASA, Department of Astrophysical and Planetary Sciences, University of Colorado, 389 UCB, Boulder, CO 80309, USA*
[2]*Institute for Astrophysical Research, Boston University, 725 Commonwealth Ave, Boston, MA 02215, USA*
[3]*Astrophysics Research Institute, Liverpool John Moores University, 146 Brownlow Hill, Liverpool L3 5RF, UK*
[4]*Center for Astrophysics | Harvard & Smithsonian, 60 Garden St., Cambridge, MA 02138, USA*
[5]*Department of Physics and Astronomy, University College London, Gower Street, London WC1E 6BT, UK*

Accepted 2022 July 10. Received 2022 July 1; in original form 2021 December 29

ABSTRACT

We investigate how the X-ray circumgalactic medium (CGM) of present-day galaxies depends on galaxy morphology and azimuthal angle using mock observations generated from the EAGLE cosmological hydrodynamic simulation. By creating mock stacks of *eROSITA*-observed galaxies oriented to be edge-on, we make several observationally testable predictions for galaxies in the stellar mass range $M_\star = 10^{10.7–11.2}\,\mathrm{M}_\odot$. The soft X-ray CGM of disc galaxies is between 60 and 100 per cent brighter along the semimajor axis compared to the semiminor axis, between 10 and 30 kpc. This azimuthal dependence is a consequence of the hot ($T > 10^6$ K) CGM being non-spherical: specifically, it is flattened along the minor axis such that denser and more luminous gas resides in the disc plane and corotates with the galaxy. Outflows enrich and heat the CGM preferentially perpendicular to the disc, but we do not find an observationally detectable signature along the semiminor axis. Spheroidal galaxies have hotter CGMs than disc galaxies related to spheroids residing at higher halo masses, which may be measurable through hardness ratios spanning the 0.2–1.5 keV band. While spheroids appear to have brighter CGMs than discs for the selected fixed $M_\star$ bin, this owes to spheroids having higher stellar and halo masses within that $M_\star$ bin, and obscures the fact that both simulated populations have similar total CGM luminosities at the exact same $M_\star$. Discs have brighter emission inside 20 kpc and more steeply declining profiles with radius than spheroids. We predict that the *eROSITA* 4-yr all-sky survey should detect many of the signatures we predict here, although targeted follow-up observations of highly inclined nearby discs after the survey may be necessary to observe some of our azimuthally dependant predictions.

Key words: methods: numerical – Galaxy: disc – Galaxy: evolution – Galaxy: formation – intergalactic medium – X-rays: galaxies.

1 INTRODUCTION

The circumgalactic medium (CGM) is the gaseous baryonic component surrounding a galaxy. Over cosmic times, these CGMs are thought to participate in the assembly and evolution of galaxies. The properties of the CGM have been observed to exhibit azimuthal dependence around highly inclined galaxies in ultraviolet (UV) absorption-line surveys. Mg II shows azimuthal dependence within ∼50 kpc such that absorption is stronger along the polar, semiminor axis, and along the equatorial, semimajor axis (Bordoloi et al. 2011; Bouché et al. 2012; Kacprzak, Churchill & Nielsen 2012; Lan, Ménard & Zhu 2014; Ho et al. 2017; Martin et al. 2019; Kacprzak et al. 2019a). It is less clear if high-excitation UV ions like O VI display a similar azimuthal dependence (Kacprzak et al. 2015, 2019b), though Beckett et al. (2021) finds O VI enhanced along the semiminor axis. The interpretation often is that UV absorption along the polar direction is preferentially tracing superwind-driven outflows, while gas along the equatorial direction is tracing inflows (e.g. Shen et al. 2013; Mitchell et al. 2020; Péroux et al. 2020), and may thus present a revealing view of the baryon cycle in action.

Soft X-ray emission around disc-like galaxies also exhibits azimuthal dependence; however, the number of detected galaxies and the detection distance from the galaxy are limited by the capability of existing X-ray telescopes. Emission from edge-on galaxies usually does not extend far beyond the optical extent of the disc, this being limited to the disc–halo interface (Li et al. 2008; Hodges-Kluck & Bregman 2013; Li et al. 2017; Hodges-Kluck, Bregman & Li 2018) and may more appropriately be considered an extended interstellar medium (ISM). While X-ray emission is observed extended above and below the discs of star-bursting galaxies (e.g. Strickland et al. 2004; Hodges-Kluck et al. 2020) indicating clear signatures of outflows (Strickland & Heckman 2009), these objects are rare outliers that are among the most luminous extended X-ray objects associated with disc galaxies.

Extended X-ray emission from gaseous haloes around typical galaxies are a general prediction of cosmological hydrodynamical

★ E-mail: benjamin.oppenheimer@colorado.edu

simulations (Toft et al. 2002; Rasmussen et al. 2009; Crain et al. 2010, 2013; Kelly, Jenkins & Frenk 2021); however, *Chandra* and *XMM-Newton* possess the sensitivity to detect emission associated with only a handful of the most massive nearby late-type galaxies (Anderson & Bregman 2011; Dai et al. 2012; Bogdán et al. 2013b, a; Anderson, Churazov & Bregman 2016; Bogdán et al. 2017; Li et al. 2017; Das et al. 2019). Newer simulations, including EAGLE (Crain et al. 2015; Schaye et al. 2015; McAlpine et al. 2016) and IllustrisTNG (Nelson et al. 2018; Pillepich et al. 2018a), have been tuned to fit some of the observed properties of galaxies. X-ray emission predictions, for both EAGLE (Davies et al. 2019) and IllustrisTNG (Truong et al. 2020), have been generated from these simulations and compared to observations of emission around galaxies, but these mainly focus on central regions and not extended emission for typical galaxies.

The *eROSITA* instrument on the Spectrum-Roentgen-Gamma mission (Merloni et al. 2012), launched in 2019 July, opens new possibilities for the detection of extended, soft X-ray emission ($\leq$2.0 keV) associated with typical galaxies. The onboard detectors have been operating within mission expectations for soft X-ray energies (Predehl et al. 2021), which means that the grasp (the product of the collecting area and the field of view) of *eROSITA* should achieve the expected signal in its primary 4-yr all-sky survey comprising eight 6-month scans (the eRASS:8 survey). *eROSITA* is predicted to detect $>10^5$ clusters and groups (Pillepich et al. 2018b), and it will also collect photons from the CGM of galaxies, but stacking methods are required to detect the emission as was done for the *ROSAT* all-sky survey (Anderson et al. 2015).

The 30$\times$ greater sensitivity of *eROSITA* compared to *ROSAT* allows the detection of extended X-ray emission associated with galaxies (Chadayammuri et al. 2022; Comparat et al. 2022). The superior spatial resolution of *eROSITA* offers a better opportunity to separate CGM emission from galactic sources, including X-ray binaries, the hot ISM, and potential active galactic nuclei (AGNs). Oppenheimer et al. (2020, hereafter O20) predicted that *eROSITA* should be able to detect soft X-ray emission in the CGM around typical galaxies in the nearby Universe at $z \lesssim 0.01$. The aim of O20 was to demonstrate that *eROSITA* could resolve diffuse X-ray haloes around galaxies with masses as low as $M_\star = 10^{10.2}\,\mathrm{M}_\odot$. Given the prediction of both the EAGLE and IllustrisTNG simulations that more highly star-forming galaxies at fixed halo mass have denser CGMs (Davies et al. 2020), O20 predicted that *eROSITA* emission should grow stronger with higher star formation rates (SFRs) at fixed stellar mass.

Here, we continue the investigation of mock *eROSITA* observations by using the EAGLE simulation to forward model observations of galaxies rotated completely inclined to appear edge-on. We define galaxy subsamples using kinematic morphology, rotating them all to be edge-on, while concentrating on more massive galaxies with $M_\star = 10^{10.7} - 10^{11.2}\,\mathrm{M}_\odot$. The purposes of our morphology-centred investigation is two-fold: (1) to determine if there is azimuthal dependence in simulated X-ray stacks of disc-like galaxies and (2) to establish whether the emission depends on morphology. The second purpose does not necessarily rely on galaxy orientation, and provides an exploration of X-ray emission as a function of morphology.

We focus on mock *eROSITA* observations, because the eRASS surveys provide all-sky coverage with consistent quality and data reduction. This contrasts with deep *XMM* and *Chandra* observations focused on individual galaxies that often fall in the category of rare outliers. By choosing stacks of $\sim$100 galaxies within morphologically similar samples, we develop an experiment to survey the appearance of typical galactic X-ray CGM profiles. We create *idealized* samples by placing the galaxies at $z = 0.005$, a distance of 22 Mpc, but in practice it will be necessary to use galaxies that either are at higher redshift, are at higher ecliptic latitudes where eRASS exposure times are longer, and/or include high inclinations as opposed to perfectly edge-on discs.

The paper is arranged as follows. Section 2 introduces the EAGLE simulation, defines the galaxy samples, and details the *eROSITA* forward modelling pipeline. The main results are presented in Section 3, first concentrating on the mock observational results in Section 3.1 and the physical interpretation within the EAGLE simulations in Section 3.2. Section 4 discusses some of the results relating to X-ray CGM properties as a function of morphology, the significance of emission along the equatorial direction, existing observations of X-ray emission around inclined galaxies, and a discussion of the similar work by Truong et al. (2021) focusing on the IllustrisTNG simulation. We summarize in Section 5.

2 METHODS

2.1 EAGLE simulations

Our analysis uses the 'Reference' EAGLE cosmological simulation (Crain et al. 2015; Schaye et al. 2015). This 100^3 comoving Mpc^3 run, referred to as Ref-L100N1504, uses initial conditions with 1504^3 collisionless dark matter (DM) and an initially equal number of smooth particle hydrodynamic (SPH) particles starting at $z = 127$. The Planck Collaboration (2013) cosmogony is used ($\Omega_\mathrm{m} = 0.307$, $\Omega_\Lambda = 0.693$, $\Omega_\mathrm{b} = 0.04825$, and $H_0 = 67.77\,\mathrm{km\,s^{-1}\,Mpc^{-1}}$). The code used is a significantly modified version of the *N*-body/Hydrodynamical code GADGET-3 last described in Springel (2005). The SPH implementation uses a pressure-entropy-based formulation (Hopkins 2013) and a series of additional modifications referred to as ANARCHY, the influence of which are explored by Schaller et al. (2015).

The EAGLE code applies a number of subgrid physics modules, including radiative cooling (Wiersma, Schaye & Smith 2009a), star formation (Schaye & Dalla Vecchia 2008), stellar evolution and metal enrichment (Wiersma et al. 2009b), super-massive black hole (SMBH) formation and accretion (Booth & Schaye 2009; Schaye et al. 2015; Rosas-Guevara et al. 2015), stellar feedback (Dalla Vecchia & Schaye 2012), and SMBH feedback (Booth & Schaye 2009). Thermal prescriptions, where the imparted feedback energy heats local SPH particles, are applied for both stellar and SMBH feedback. Crain et al. (2015) describes how the calibration of these feedback schemes credibly reproduces the galactic stellar mass function and galaxy sizes.

The EAGLE simulation has a mass resolution for DM particles of $9.7 \times 10^6\,\mathrm{M}_\odot$ and for SPH particles of $1.8 \times 10^6\,\mathrm{M}_\odot$. This resolution has a Plummer-equivalent softening length of 700 proper pc at $z < 2.8$, and 2.66 comoving kpc at $z > 2.8$. The interparticle SPH separation is $3.8 \times (n_\mathrm{H}/(10^{-3}\mathrm{cm}^{-3}))^{-1/3}$ kpc.

EAGLE haloes are identified via a two-step process, starting with a friends-of-friends algorithm linking DM particles within a length of 0.2 the mean interparticle separation, and linking associated gas and star particles to the nearest DM particle. The SUBFIND algorithm (Springel et al. 2001; Dolag et al. 2009) then identifies bound substructures within the haloes, and the halo mass is characterized by the spherical overdensity mass (M_{200}) centred on the halo's most bound particle.

2.2 Galaxy subsamples

To generate observationally reproducible samples, we select simulated central galaxies based on stellar mass and kinematically

Table 1. EAGLE galaxy kinematic morphology sample ranges for $M_\star = 10^{10.7}$–$10^{11.2}$ $M_\odot$.

Sample	κ1	κ2	κ3	κ4	κ4-med-discs
κ Low	0.114	0.202	0.322	0.477	0.477
κ High	0.201	0.321	0.475	0.767	0.767
$\log\langle M_{200}\rangle^a$	12.88	12.88	12.75	12.58	12.46

[a] Mean M_{200}.

defined morphology that has been shown to accurately correspond to direct measures of morphology (Thob et al. 2019). We focus on the mass range of $M_\star = 10^{10.7-11.2}$ $M_\odot$, which is a bin of width 0.5 dex that O20 labelled as the 'high-mass' sample. EAGLE has 498 galaxies in this mass range within its 10^6 Mpc^3 volume. Haloes with $M_{200} > 10^{13.3}$ $M_\odot$, which are often considered groups, are excluded because we expect the CGM of such galaxies to be individually detectable with *eROSITA*.

The resulting sample has 429 central galaxies in the given mass range for EAGLE, which is divided into quartile subsamples, each of 107 galaxies, using their kinematic morphologies. We use the definition of κ, which is the fraction of stellar kinetic energy invested in corotation,[1] to define our samples listed in Table 1. Correa & Schaye (2020) showed in an EAGLE comparison to the Sloan Digital Sky Survey that discs generally have $\kappa > 0.35$ and spheroids have $\kappa < 0.25$. We use the κ values calculated by Davies et al. (2020) using the routines of Thob et al. (2019).

The κ4 sample is clearly within the disc regime, thus we refer to this sample as 'discs.' κ1 is safely within the spheroid regime, and we refer to them as 'spheroids.' The κ2 and κ3 samples are intermediate. The left-hand panel of Fig. 1 shows that κ correlates with specific SFR (sSFR≡SFR/$M_\star$), albeit with significant scatter. As in O20, we select our samples based on observationally derivable galaxy properties, which in this case are $M_\star$ and κ, since as shown by Thob et al. (2019) κ correlates strongly with the observable ratio of rotational and dispersion velocities ($v_{\rm rot}/\sigma$). Thob et al. (2019) showed that the Spearman rank-order correlation coefficient of $v_{\rm rot}/\sigma$ to κ is 0.97. $v_{\rm rot}/\sigma$ of <0.2 and ≥1.0 correspond to the κ1 and κ4 samples, respectively.

The right-hand panel of Fig. 1 shows the gas mass fraction of CGM, defined as

$$f_{\rm CGM} \equiv \frac{M_{\rm gas}(R < R_{200})}{M_{200}(R < R_{200})} \times \frac{\Omega_{\rm M}}{\Omega_{\rm b}}, \quad (1)$$

and the halo mass, M_{200}, properties that are easily definable in a simulation, but which are almost always observationally elusive. The median M_{200} is higher for spheroids ($10^{12.78}$ $M_\odot$ for κ1) than for discs ($10^{12.48}$ $M_\odot$ for κ4). Across the whole data set, $f_{\rm CGM}$ increases as a function of M_{200}, though since each subsample spans a wide range in M_{200} their median $f_{\rm CGM}$ values are similar. At fixed halo mass, discs occupy more gas-rich haloes than spheroids, a correlation shown for the whole EAGLE Ref-L100N1504 population by Davies et al. (2020).

2.2.1 *Rotating galaxies*

Every galaxy is rotated edge-on using the angular momentum axis calculated from all stars within 30 kpc of its centre. We perform this even for spheroid galaxies, but we will show there is no preferred alignment in any property we explore for the spheroids. All images place the angular momentum axis vertically, and the disc axis horizontally. We use a coordinate system of $\phi = 0 - 90°$ with 0° (90°) being the semimajor equatorial (semiminor polar) axis. For disc galaxies, cosmologically based simulations generally indicate accretion along the semimajor axis (Stewart et al. 2017; Ho, Martin & Schaye 2020; Trapp et al. 2022) and superwind outflows along the semiminor axis (Shen et al. 2013; Mitchell et al. 2020; Péroux et al. 2020).

2.2.2 *The κ4-med-discs sample*

We create a separate 'medium discs' or med-discs sample of 30 κ4 galaxies human-classified based on their morphologies. Three people, E. Huscher, A. Nica, and B. Oppenheimer, visually classified the galaxies using their total gas maps. We (i) determined if the galaxies are rotated to be well-aligned edge-on, (ii) rejected galaxies with obvious gas-rich satellites, and (iii) estimated the size of the discs with a score between 1 (small) and 3 (large). We aggregated the scores and determined that the intermediate-sized discs are most comparable to typical spiral galaxies with H VI discs, such as NGC 891. Smaller discs are compact spirals often with centralized star formation, and larger discs are often diffuse, flocculent, and/or warped, which are often in higher-mass haloes.

The human classification of the κ4-med-discs sample created some surprisingly rigid data cuts. While the median halo mass is not that much lower than the κ4 sample, cf. $M_{200} = 10^{12.45}$ and $10^{12.48}$ $M_\odot$, the mean mass is 0.12 dex lower as listed in Table 1 with a total range spanning $10^{12.20-12.75}$ $M_\odot$, which excises the 13 most massive κ4 haloes. The total sSFR range is $10^{-10.58}$–$10^{-10.00}$ yr^{-1}, which is a much narrower range than Fig. 1 shows for κ4 and excises the 29 least star-forming galaxies.

2.3 Forward modelling pipeline

The forward modelling pipeline we use was introduced in §2.3 of O20. We use the PYXSIM package[2] (ZuHone & Hallman 2016) to create mock SIMPUT[3] files. For each SPH particle with $T > 10^{5.3}$ K and hydrogen number density $n_{\rm H} < 0.22$ cm^{-3} inside 3 R_{200}, PYXSIM generates a Monte Carlo random sampling of photons using X-ray spectra from the Astrophysical Plasma Emission Code (APEC; Smith et al. 2001). APEC assumes collisional ionization equilibrium given the density, temperature, and metallicity (including nine individually tracked abundances) of each SPH particle. Like O20, we do not simulate X-rays from the ISM. The photons from the galaxy's CGM are termed 'source' photons.

We place the simulated galaxies at $z = 0.005$, corresponding to a distance of 22.2 Mpc for our *eROSITA* mocks. We include simulated Galactic foreground emission and a Cosmic X-ray background (CXB) randomly generated using the SOXS package.[4] Galactic absorption assuming a column of $N_{\rm HI} = 2 \times 10^{20}$ cm^{-2} is then applied.

The SIXTE simulation software (Dauser et al. 2019) uses SIMPUT file inputs to create mock 2 kilosecond *eROSITA* observations with instrumental background centred on the position of the galaxy. Event files are created using the `erosim` tool for the seven *eROSITA* cameras and combined into one image (see fig. 1 of O20). Individual

[1] The variable $\kappa_{\rm co}$ is often used in other publications in place of κ.

[2] http://hea-www.cfa.harvard.edu/~jzuhone/pyxsim/pyXSIM is an implementation of the PHOX algorithm (Biffi et al. 2012; Biffi, Dolag & Böhringer 2013).

[3] http://hea-www.harvard.edu/heasarc/formats/simput-1.1.0.pdf

[4] http://hea-www.cfa.harvard.edu/~jzuhone/soxs/; background described in http://hea-www.cfa.harvard.edu/~jzuhone/soxs/users_guide/background.html

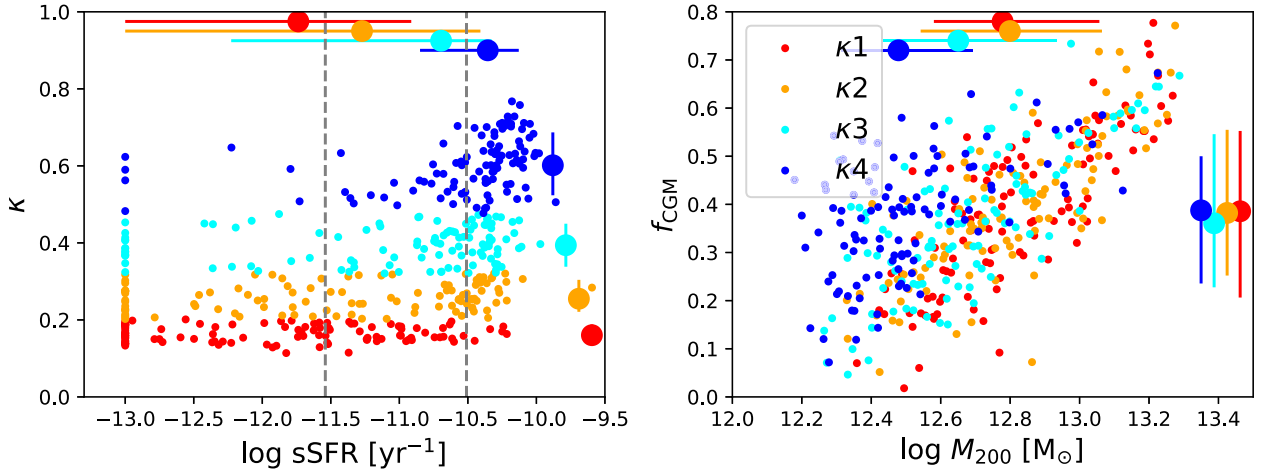

Figure 1. Our EAGLE galaxy subsamples, coloured from red to blue for $\kappa 1$ (spheroids) to $\kappa 4$ (discs). The left-hand panel plots two galaxy characteristics for the $M_\star = 10^{10.7-11.2}$ M$_\odot$ samples. sSFR correlates with κ. sSFR $\leq 10^{-13}$ yr^{-1} are plotted as having 10^{-13} yr^{-1}. The right-hand panel plots two halo-wide characteristics, virial mass versus f_{CGM}, which is the fractional gas content of the CGM relative to its expected total baryon content. Large circles and error bars on the top and to the right show the median and 1σ dispersion for each distribution. The dashed lines in the left-hand panel indicate the low-sSFR (left of left line) and high-sSFR (right of right line) samples of O20.

CXB compact sources are common within each mock observation, therefore we use the CIAO (Fruscione et al. 2006) `wavdetect` routine to detect and mask compact sources, including CXB sources, bright satellites, and point-source-like emission from dense gas at the position of the galaxy. We mainly report on extended emission beyond a projected radius of $r \gtrsim 10$ kpc, but plot emission profiles to 5 kpc. We include only non-star-forming gas with density $n_H < 0.22$ cm^{-3}, because our focus is mainly on extended CGM emission as in O20. These higher density regions correspond to locations of ISM gas, as well as the stellar component, which includes X-ray binary emission, both of which we also do not attempt to simulate. Hence, our designed experiment aims to resolve CGM gas and works only at lower redshifts.

Individual masked images with 9.6 arcsec pixels are added together in our mock stacks, as are the individual exposure maps that include the `wavdetect`-generated masks. We make an off-source 'bkgd' stack using the same procedure performed without CGM emission. Both stacks with photon counts are divided by their respective summed exposure ('expo') maps (in seconds) to obtain a 'signal' photons s^{-1} map, using photons$_{source}$/expo$_{source}$ − photons$_{bkgd}$/expo$_{bkgd}$. We convert to photons s^{-1} arcmin^{-2} as our primary unit. The four signal maps of 107 galaxy stacks are shown in Fig. 2 with the disc plane aligned horizontally.

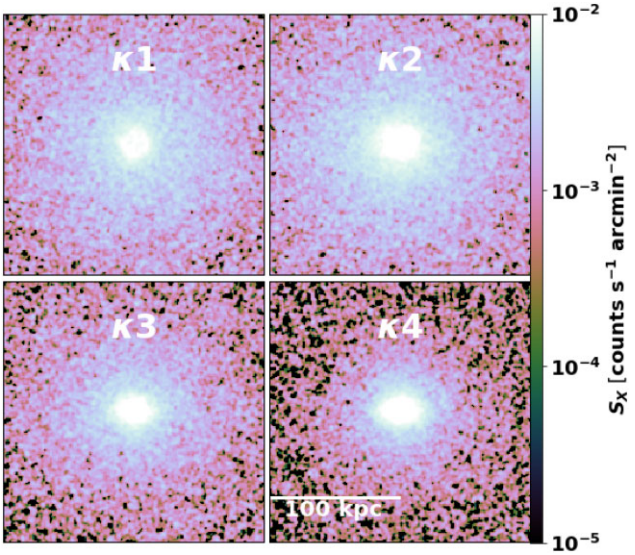

Figure 2. Soft X-ray photon flux of $\kappa 1$ (top left), $\kappa 2$ (top right), $\kappa 3$ (bottom left), and $\kappa 4$ (bottom right) X-ray maps in the 0.2–1.5 keV energy band. The flux becomes more elliptical along the semimajor axis at greater κ.

2.3.1 *Frequency of edge-on galaxies in the observed sky*

Although we place the simulated galaxies at 22.2 Mpc, this is far too nearby to find 10^2 edge-on galaxies. O20 placed galaxies at $z = 0.01$ with random orientations, noting that one expects there to be 70 galaxies for our mass range at an average distance of 44.6 Mpc ($z = 0.01$) across the entire sky with galactic latitude $|b| > 15°$. Unlike O20, our strategy does not yield a wholly realistic observational sample. Being an average of 2× closer at $z = 0.005$, this reduces the amount of galaxies by 8× to 10 total galaxies. If we assume that galaxies must have inclinations above $i = 75°$ to be considered edge-on, which corresponds to 26 per cent of galaxies, this leaves an expectations of just above 2 galaxies in our mass range at a volume-weighted average redshift of $z = 0.005$. Hence, there exists nearly a 50× difference between our simulated and a realistic sample in the eRASS:8 survey.

There are a couple ways to approach our simulated sample. We could motivate the need to observe several nearby edge-on galaxies for a total of 200 kiloseconds after the 4-yr eRASS:8 survey to achieve the expected throughput. This could be an efficient experiment given *eROSITA*'s lower and more stable background as well as its superior grasp compared to *XMM-Newton*. However, this does not produce a statistical ensemble using so few galaxies.

For a larger sample, we can extend to higher redshift given our goal of resolving outside $r = 10$ kpc. Using *eROSITA* resolution of 15 arcsec, we can include galaxies up to a higher redshift, $z \approx 0.03$. This allows ≈200× more galaxies with $i > 75°$, which creates an ensemble stack of ≈500 galaxies with resolvable CGM emission. The trade-off is that the signal per galaxy declines by distance squared,

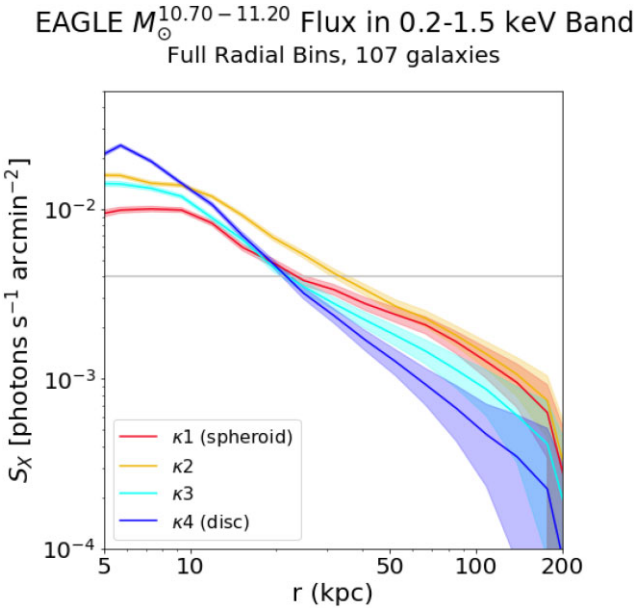

Figure 3. The flux across the entire 0.2–1.5 keV band as a function of radius for the four subsamples with shading indicating 1σ Poisson errors from the source and background stacks added in quadrature. Rotationally supported disc galaxies have greater flux at small radii than dispersion-dominated spheroid galaxies. All profiles decline in flux at larger radii, however, dispersion-dominated galaxies decline more slowly. The total astrophysical and instrumental background at 0.2–1.5 keV is indicated by grey line.

and the signal is still $\sim 10\times$ too low for eRASS:8. Therefore, for the stacked results in Section 3.1.2, it is helpful to keep in mind that error ranges may be $3\times$ larger for a realistic sample from eRASS:8 assuming Poisson statistics.

3 RESULTS

In this section, we begin by discussing results of the mock observations in Section 3.1. We focus on the general trends of our four subsamples of galaxies first, and then discuss the azimuthal dependence of X-ray emitting gas around aligned discs. Within this section, we discuss global quantities of the galactic haloes, including M_{200} and $f_{\rm CGM}$. We then explore the physical characteristics within the EAGLE simulations in Section 3.2 to understand the state of the CGM that gives rise to the results in Section 3.1.

3.1 Mock observational results

Fig. 2 demonstrates that spheroid-dominated galaxies in $\kappa 1$ and $\kappa 2$ have more extended emission than the disc sample in $\kappa 4$. When we plot surface brightness (SB) radial profiles in Fig. 3, we see $\kappa 1$, $\kappa 3$, and $\kappa 4$ form a progression of declining SB at large radius (beyond 20 kpc), but increasing interior emission (within 20 kpc). The interior emission is generally more associated with the feedback-driven baryon cycle of gas outflowing, recycling, and accreting (e.g. Mitchell et al. 2020), while the exterior emission is more likely to arise from a quasi-static hot halo (e.g. Oppenheimer 2018). Discs therefore have steeper radial X-ray profiles than spheroids. We predict the flux of spheroids at 100 kpc is 1.3×10^{-3} compared to 5×10^{-4} photons s^{-1} arcmin^{-2} for discs, and that our experiment should be able to distinguish the two, given the shaded Poisson error bar ranges generated from source plus background noise counts added in quadrature. These levels lie below the total instrumental plus astrophysical background of 4×10^{-3} photons s^{-1} arcmin^{-2} plotted in grey, which indicates the necessity of stable background subtraction to reveal the signal.

The overall luminosities between 10 and 150 kpc for these X-ray CGMs using the 0.2–1.5 keV band are $10^{40.9}$ erg s^{-1} for $\kappa 1$ and $10^{40.6}$ erg s^{-1} for $\kappa 4$. While the extended emission from spheroid CGMs averages double the luminosity of disc CGMs in the $M_\star = 10^{10.7-11.2}$M$_\odot$ bin, in Section 4.1, we discuss that the bias of shifted stellar mass distributions within this bin does not necessarily indicate brighter spheroid haloes at a specific $M_\star$. We also find more X-ray luminosity in the interior 10 kpc for discs than spheroids (cf. $10^{39.6}$ and $10^{39.3}$erg s^{-1}), but we caution that this emission will likely be drowned out by X-ray binaries, hot ISM, and potential galactic AGN in real observations.

Finally, the $\kappa 2$ sample is out of sequence with brighter emission than this sequence expects. This in part owes to this subsample having a slightly more massive average halo than the $\kappa 1$ subsample. We discuss in Section 4.1 how M_{200} and $f_{\rm CGM}$ are the best predictors for X-ray CGM luminosity.

3.1.1 *Energy bands*

We next break down the emission by energy band, where we selected three energy bands (0.2–0.5, 0.5–0.8, and 0.8–1.5 keV) that have approximately equal numbers of photons in our *eROSITA* mocks.[5] We select these bands to optimize the division of galactic emission, which differs from the 0.3–0.6, 0.6–1.0, and 1.0–2.3 keV bands used in the *eROSITA* all-sky map press release.[6]

Fig. 4 plots the $\kappa 1$ and $\kappa 4$ samples in red and blue, respectively, with darker profiles indicating harder energy bands. Harder X-ray emission contributes more of the SB in the interior, with the two softer bands contributing relatively more in the exterior, and also in the interior of spheroids.

We plot the hardness ratio of the 0.8–1.5 keV band divided by the 0.2–0.5 keV band in Fig. 5. The extended CGMs of spheroids are harder, while the interior emission around discs is harder. The overlapping 1σ Poisson errors of this ratio indicate this is a challenging measurement. Furthermore, this ratio is not very sensitive to temperature, being primarily affected by metal emission that contributes disproportionally to the 0.8–1.5 keV, especially in the cooler gas around discs, but we will discuss that there are still indications of differing temperature structures in Section 3.2. Achieving a measurement of temperature may instead require a microcalorimeter instrument with much higher spectral resolution than *eROSITA*'s silicon-based CCDs.

3.1.2 *Azimuthal dependence*

We now divide the galaxy into azimuthal regions to explore the orientation dependence of X-ray emission around edge-on galaxies, which is more pronounced in the disc galaxy sample. We define two regions: the 'equatorial' direction along the semimajor axis and the 'polar' direction along the semiminor axis. We attempt different opening angles, including $\Phi = \pi/2$, which includes all emission

[5] In practice, the 0.2–0.5 keV band is going to be highly dependent on Galactic absorption, which is assumed to be $N_{\rm HI} = 2 \times 10^{20}$ cm^{-2}. Owing to this absorption and *eROSITA*'s declining response below <0.5 keV, most source photons do not get counted.

[6] https://www.mpe.mpg.de/7461761/news20200619

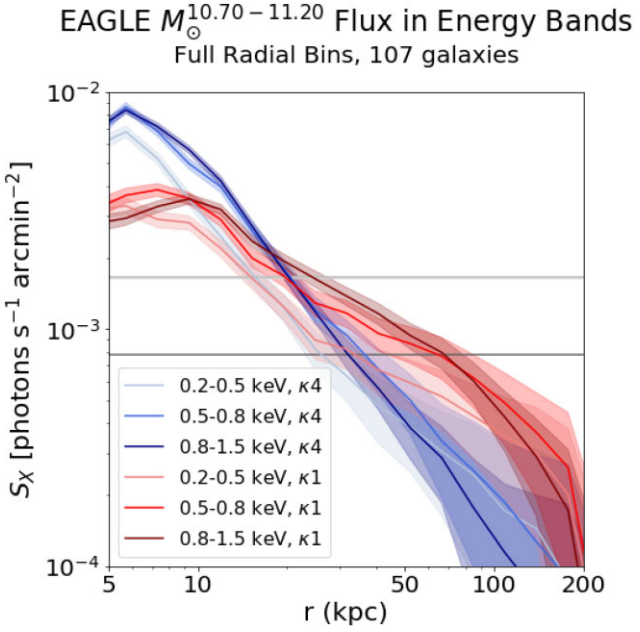

Figure 4. Flux as a function of radius for rotationally supported $\kappa 4$ and dispersion-dominated $\kappa 1$ galaxies divided into three energy bands. The flux in all three energy bands of $\kappa 4$ is greater than $\kappa 1$ at inner radii and declines at outer radii. Background levels for individual bands are indicated by increasingly darker grey lines for higher energies (the 0.2–0.5 and 0.5–0.8 keV bands overlap).

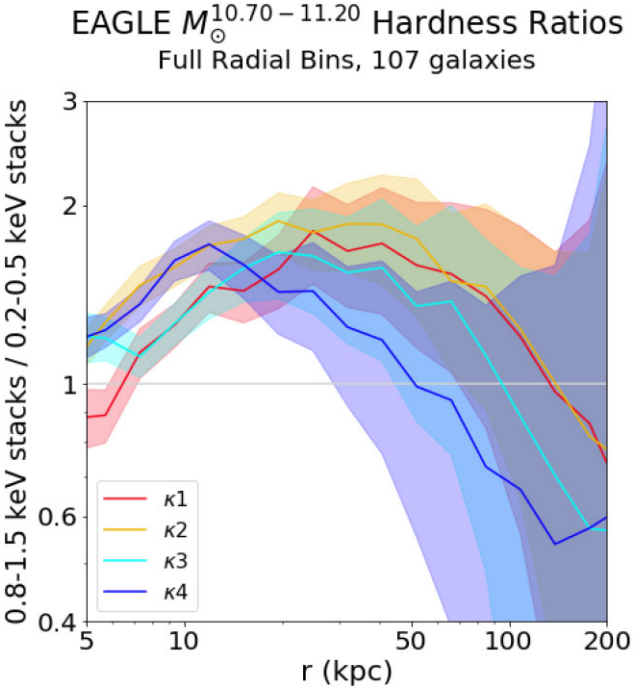

Figure 5. Hardness ratios (ratio of highest-energy stacks to lowest-energy stacks) of the galaxy subsamples. The Poisson errors here show how difficult it is to distinguish hardness ratios between samples, although the $\kappa 4$ sample does indicate hotter gas in the centre, while the spheroid samples have hotter gas in their exteriors than discs.

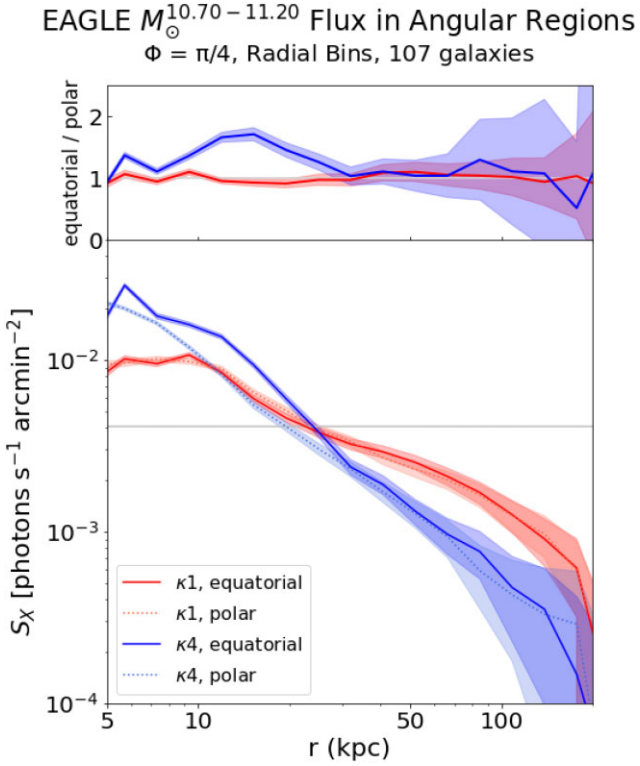

Figure 6. Flux across the 0.2-1.5 keV band divided into equatorial and polar axis regions using $\Phi = \pi/4$ regions. Disc galaxies ($\kappa 4$) show greater flux along equatorial than polar regions from 10 to 30 kpc. Spheroidal galaxies ($\kappa 1$) unsurprisingly do not show any azimuthal dependence, even though they are rotated according to their stellar kinematics. The top panel shows the ratio of the equatorial to polar emission.

within the polar and equatorial directions, as well as smaller opening angles. A smaller opening angle yields a greater difference between the equatorial and polar regions for disc galaxies that show azimuthal dependence, since smaller angles more exclusively capture the edges of the edge-on galaxies in the equatorial region and the outflows in the polar region, so the azimuthal dependencies are not 'averaged out' by the intermediate regions. We choose to focus our results using $\Phi = \pi/4$, which includes angles between $\phi = 0$–22.5° and 67.5–90° while discarding the intermediate angles.

Fig. 6 shows the equatorial and polar SB radial profiles for the spheroids and discs. While we do not see any dependence for the spheroids, as expected, we recover a clear azimuthal dependence for the discs. The equatorial axis is brighter between 5 and 30 kpc, as much as 60 per cent (0.2 dex) at $r \approx 15$ kpc, as indicated by the ratio in the top panel. We also note that the elongation is visible in the Fig. 2 $\kappa 4$ stack.

In Fig. 7, we show that the 30 med-discs sample exhibits greater azimuthal SB dependence, although weaker overall luminosity, because this sample is preferentially devoid of the more massive haloes of the $\kappa 4$ sample; the mean halo mass is $M_{200} = 10^{12.46}\,\mathrm{M}_\odot$ versus $10^{12.58}\,\mathrm{M}_\odot$ for the entire $\kappa 4$ sample. We selected the med-discs sample for a cleaner sample of edge-on galaxies, and we find that the azimuthal dependence is greater, with more emission along the disc axis.

Even though we are using fixed stellar mass bins, the average halo mass is two times higher for $\kappa 1$ than for $\kappa 4$ from Table 1. To separate out the effect of halo mass on azimuthal dependence, we stack reduced subsamples of 30 $\kappa 1$ and $\kappa 4$ galaxies in Fig. 8, with

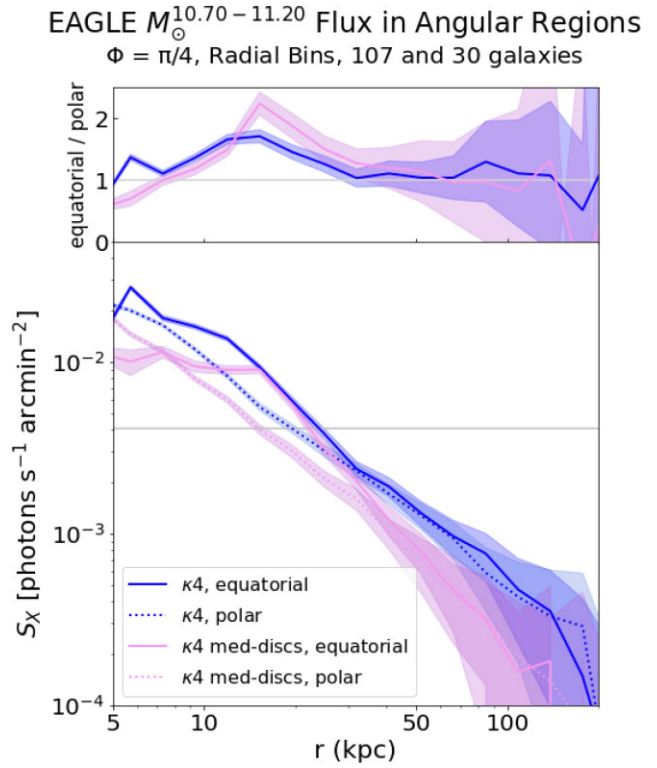

Figure 7. The 30 galaxy med-discs sample, selected to be similar to some of the most well-observed edge-on discs from the $\kappa 4$ sample, is shown in purple. Longer exposures are used to match the same total exposure time of the $\kappa 4$ sample. The azimuthal dependence is greater than the $\kappa 4$ sample, with the equatorial flux being double the polar flux at ∼15 kpc.

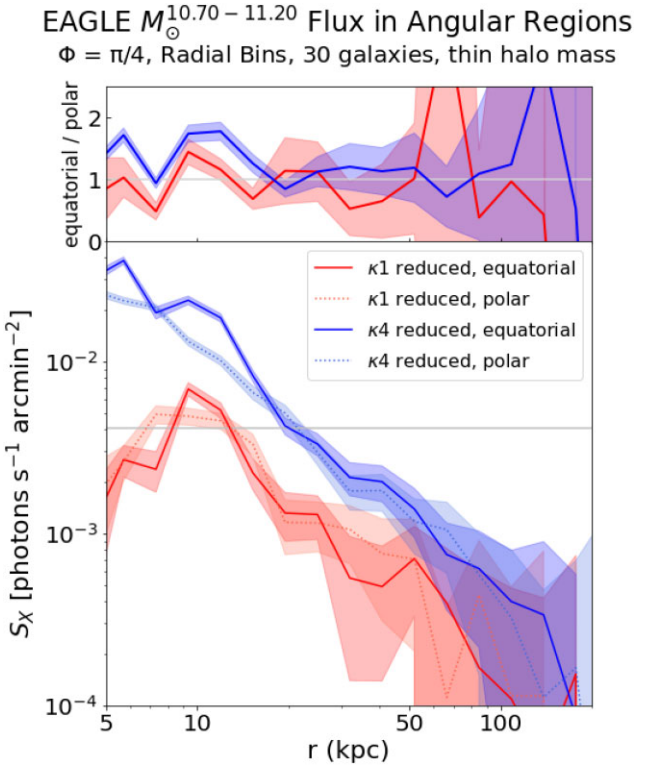

Figure 8. Stacks of 30 galaxies within a thin halo mass range, $M_{200} = 10^{12.49-12.71}$ M$_\odot$, to isolate the effect of morphology independent of halo mass dependence. The $\kappa 4$ sample shows a similar split between the equatorial and polar regions as Fig. 6, while the $\kappa 1$ sample is dimmer with larger errors.

$M_{200} = 10^{12.49-12.71}$ M$_\odot$. The equatorial flux peaking at $r \approx 15$ kpc for the reduced $\kappa 4$ sample still exists. The reduced $\kappa 1$ sample is much dimmer at all radii due to preferentially excising the massive haloes, and does not show a clear azimuthal signature. These fixed halo mass samples reiterate the results of Davies et al. (2019, 2020) that X-ray luminosity at fixed halo mass reflects the decline in $f_{\rm CGM}$ from disc to spheroid galaxies.

The brighter equatorial emission beyond the optical disc of the galaxy may be surprising if one expects more X-rays from bipolar outflows. In fact, Truong et al. (2021) does find brighter polar emission at greater radii in IllustrisTNG and EAGLE, which we discuss in Section 4.4. Observationally, bipolar outflows have been observed around star-bursting galaxies, extending out to 5–10 kpc as in the case of M82 and NGC 253 and others (Strickland et al. 2004), and even out to 30 kpc in the recent results of NGC 3079 (Hodges-Kluck et al. 2020). More typical galaxies do not as often exhibit extended bipolar emission, although bipolar outflows are sometimes observed on smaller scales as in M31 (Bogdán & Gilfanov 2008). Our prediction of equatorially enhanced emission occurs at a larger-scale (10–30 kpc), which is mainly below the detection threshold of X-ray CGMs around other edge-on galaxies, although deep *XMM-Newton* observations by Hodges-Kluck et al. (2018) for NGC 891 may provide upper limit constraints, already, as we discuss in Section 4.3.

Finally, we have explored hardness ratios in azimuthal regions, but did not detect any observationally detectable variation. While this may reflect the weak azimuthal temperature dependence as we will explore in the next subsection, a microcalorimeter instrument may be able to measure temperature via emission-line ratios.

3.2 Physical properties

We now discuss the underlying physical properties of the hot gas that give rise to the X-ray emission around the stacked galaxies. We begin by looking at averaged maps and then move to radial profiles.

3.2.1 Physical property maps

The gas density maps in Fig. 9 (left-hand panels) include gas only above $T = 10^{5.3}$ K (the cut-off temperature of the APEC tables). In addition to subtle changes, these maps show an obvious disc-like structure in the $\kappa 4$ map, which has slightly lower extended gas density as well. The extended $\kappa 4$ hot CGM has some ellipticity along the disc axis. The temperature maps (middle panels) show far more variation, and the lower temperatures around disc galaxies are a sign of their lower halo masses in Fig. 1. There exists little azimuthal dependence in temperature beyond the disc. The metallicity maps, again of only the $T \geq 10^{5.3}$ K gas and normalized to solar using Asplund et al. (2009) abundances, in the right-hand panels show a polar enhancement indicating enrichment by bipolar outflows for the $\kappa 4$ sample. Crain et al. (2013) stacked GIMIC galaxies in much the same way, but did not see bipolar metal outflows in these simulations with only stellar feedback that was weaker than EAGLE's prescription. We note similar trends in EAGLE as seen in IllustrisTNG by Truong et al. (2021), which we discuss further in Section 4.4.

3.2.2 Azimuthal radial profiles

We now divide the physical property maps into $\Phi = \pi/4$ regions, as we did for the flux maps in Section 3.1.2, and plot equatorial and

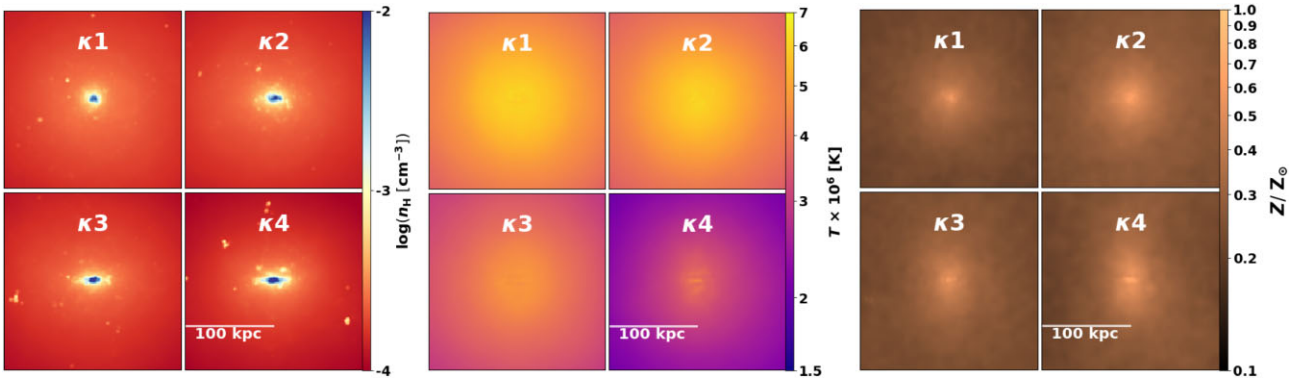

Figure 9. Physical property stacked maps of the hot gas within 200 × 200 kpc panels: hydrogen number density (left-hand panels), temperature (middle panels), and metallicity (right-hand panels). Each panel set shows the four subsamples: $\kappa 1$ (top left), $\kappa 2$ (top right), $\kappa 3$ (bottom left), and $\kappa 4$ (bottom right). Higher κ galaxies have more elliptical extended gas CGMs beyond the disc, which are slightly lower density than spheroids. The temperature panels show cooler gas around discs than spheroids, indicative of discs living in lower mass haloes. Bipolar metal-enriched outflows are apparent in disc galaxies.

polar regions for the $\kappa 1$ and $\kappa 4$ stacks in Fig. 10. As expected, only $\kappa 4$ shows azimuthal dependence, quantified as a ratio in the top panels. The density (left-hand panel) indicates the most significant difference with 2.4 × (1.6×) higher density along the equatorial direction than the polar direction at 15 (20) kpc. The temperatures (central panel) do not show significant azimuthal dependence, while the metallicity (right-hand panel) is enhanced along the bipolar outflow direction at CGM distances.

It is interesting that the greatest difference is in density, and if X-ray emission is scaled by density squared, one may expect an even larger difference than the 60 per cent difference at 15 kpc. The slightly lower metallicity is not enough to explain the difference. First, the distribution of physical properties (i.e. individual gas particles in the simulation) determines X-ray emission, and not the average. Additionally, we apply the `wavdetect` algorithm to excise point-like sources, even if they arise from dense concentrations of CGM gas, which could boost average density but not contribute to X-ray emission.

4 DISCUSSION

Our main results are that (1) the X-ray CGM of spheroidal galaxies in a fixed stellar mass bin appear more luminous than that of discs, and (2) edge-on discs exhibit azimuthal dependence where X-ray emission is brighter along the equatorial axis than the polar direction.

4.1 Why spheroids appear to have brighter X-ray CGMs than discs

O20 defined the extended X-ray emission as beyond 10 kpc, $L_{X,>10\mathrm{kpc}}$, finding that high-sSFR CGMs are brighter than their low-sSFR counterparts, although the difference is small ($\lesssim 0.1$ dex) for the O20 EAGLE high-mass samples. However, our morphological samples show that spheroids have an average $L_{X,>10\mathrm{kpc}} = 10^{40.9}$ erg s^{-1} that is double the brightness of discs with $L_{X,>10\mathrm{kpc}} = 10^{40.6}$ erg s^{-1}.[7] Given that discs (spheroids) are generally star forming (passive), this duality in average extended luminosities presents a paradox – how do both high-sSFR and spheroids possess brighter X-ray CGMs?

O20 performed linear regressions on the halo properties that are most predictive for X-ray luminosity (their fig. 4), and found that a relation where

$$L_{X,>10\mathrm{kpc}} = L_{X,0} M_{200}^{\alpha} f_{\mathrm{CGM}}^{\beta} \quad (2)$$

well-describes extended X-ray CGM emission. In this formulation, α ranged between 1.2 and 1.6 for EAGLE and IllustrisTNG haloes hosting $M_\star \approx 10^{10.2-11.2}$ M$_\odot$ galaxies with $\alpha = 1.2$ being the relation for the EAGLE sample we explore here, and β ranged between 1.6 and 2.0 with $\beta = 2.0$ for our sample. Hence, the total gas fraction inside R_{200} is a greater determinant than halo mass, especially for the EAGLE high-mass sample. As discussed in Section 2.2 using Fig. 1, both the median and mean M_{200} is 0.3 dex higher for spheroids while median f_{CGM} is similar; therefore it is consistent with equation (2) that the spheroids having ∼0.3 dex brighter luminosities owes mainly to halo mass. Compare this to the O20 sSFR division, where the high-sSFR bin has a median f_{CGM} that is 0.13 dex higher and M_{200} that is 0.10 dex lower versus the low-sSFR sample; therefore the high-sSFR sample is just slightly (∼0.1 dex) brighter according to equation 2 that supports the O20 result.

While the spheroids appear brighter than discs owing to higher halo masses, even within fixed $M_\star$ bins that span a factor of three in mass, the distributions of stellar masses are not uniform. We plot individual $L_{X,>10\mathrm{kpc}}$ values calculated directly from the SIMPUT files[8] as a function of $M_\star$ in Fig. 11. We find no obvious trend of luminosity with morphology at fixed $M_\star$. Instead, the distribution of stellar masses within the bin is the most important determinant for the average κ sample luminosity, with $\kappa 2$ ($\kappa 4$) having the most (least) massive galaxies. Therefore, we find that spheroids *at fixed specific* $M_\star$ are not necessarily brighter than discs in EAGLE. Higher stellar masses are indicative of higher halo masses for our stellar mass-defined samples.

As a consistency check, the squares plotted in Fig. 11 are the mean $L_{X,>10\mathrm{kpc}}$ values for each morphological sample calculated from the SIMPUT files. They agree with the $L_{X,>10\mathrm{kpc}}$ values from the forward-modelled SB profiles in Fig. 3 within 0.1 dex, demonstrating that our stacking method recovers the true answer from the simulation.

This exercise using a simulation where we know the answers provides a cautionary tale when interpreting observations. The

[7] We integrate luminosities between 10 and 150 kpc using the 0.2–1.5 keV band, which is shifted from the O20 using 10–200 kpc and the 0.5–2.0 keV band, but are of comparable luminosity.

[8] As in O20 fig. 4, we take luminosities calculated by PYXSIM before they are put through the SIXTE instrument simulator.

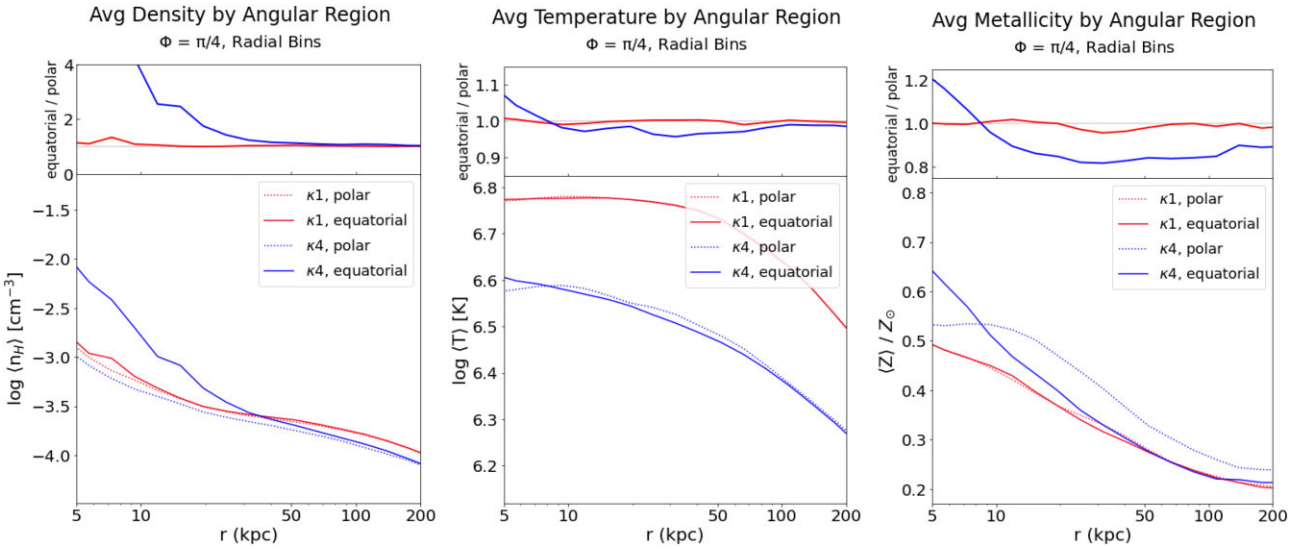

Figure 10. Projected radial profiles in polar and equatorial azimuthal bins of physical quantities for the $\kappa 1$ and $\kappa 4$ samples. Mean density, temperature, and metallicity are displayed from left to right. $\kappa 1$ stacks show no azimuthal dependence as expected, while the $\kappa 4$ stacks show several differences, the most significant being density. Metallicity, normalized using $Z_\odot = 0.0142$, is enhanced along the polar direction indicating outflowing gas. The top panels show the ratio of the equatorial-to-polar values.

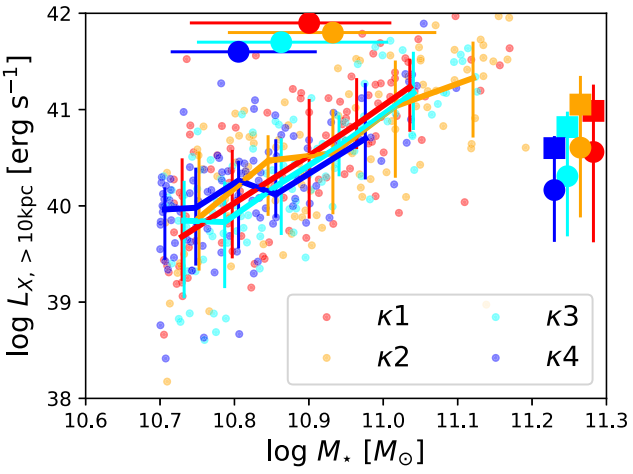

Figure 11. Extended (>10 kpc) X-ray emission as a function of stellar mass divided into our four morphological samples with points showing individual galaxies and solid lines showing medians. Lines are adaptive bins that divide the 107-galaxy samples into five equally sized $M_\star$ bins with vertical error bars showing the 1σ spread. There is no obvious trend for $L_{X,>10\mathrm{kpc}}$ on morphology at fixed $M_\star$. Large circles and error bars on the top and to the right show the median and 1σ dispersion for each distribution. Brighter spheroid haloes have a higher distribution of $M_\star$ than disc haloes. Large squares indicate the mean $L_{X,>10\mathrm{kpc}}$.

spheroid CGMs, which appear double the brightness as their disc counterparts, are not necessarily brighter at a specific $M_\star$. This demonstrates that it is possible to reach a false conclusion through stacking; however, one can subdivide their samples many different ways (e.g. different stellar mass bins in this case) to test the robustness of their conclusions when working with real observations where one does not have the answer from individual galaxies.

Related to this point, one might also get the impression that f_{CGM} is insensitive to morphology from the nearly identical median f_{CGM} for the four samples in Fig. 1. However, as clearly shown in Fig. 8 (and by Davies et al. 2020), spheroids in fact have lower f_{CGM} than discs at fixed halo mass. The similar median f_{CGM} values across the samples occur because spheroids have below-average f_{CGM} values at higher M_{200}, while discs have above-average f_{CGM} values at lower M_{200}. At fixed halo mass, the CGM around discs is *brighter* than that around spheroids, however, in our kinematically defined samples, the effect of halo mass causes spheroids to appear brighter.

4.2 Equatorially enhanced X-ray emission

Our prediction that extended diffuse X-ray haloes at 10–30 kpc should be brighter along the semimajor axis of their host galaxies provides a key test for future *eROSITA* observations. The prediction is related to the dynamical state of hot gaseous haloes that deviate from spherical hydrostatic equilibrium by having net rotation along the disc axis (Oppenheimer 2018). Given the observation that the Milky Way gaseous hot halo may be rotating (Hodges-Kluck, Miller & Bregman 2016), a set of analytical models for rotating hot haloes with enhanced densities along the disc axis was developed by Sormani et al. (2018).

We show the velocity maps for the the $\kappa 1$, $\kappa 4$, and $\kappa 4$-med-discs samples in Fig. 12. Indeed, there is net rotational velocity in these galaxies that were rotated and stacked to have their angular momentum vectors aligned. While CCD-based X-ray instruments like *eROSITA* will likely not be able to observe these velocities in the foreseeable future, a microcalorimeter mission focused on the CGM could measure the azimuthal velocity dependence, which has important implications for how disc galaxies accrete material from the hot CGM. If we consider the precipitation criterion of $t_{\mathrm{cool}}/t_{\mathrm{ff}} \lesssim 10$ (Sharma et al. 2012) for gas to cool, the rotating models of Sormani et al. (2018) favour condensation of cool gas near the disc axis by (i) lowering the cooling time (t_{cool}) with increased density, and (ii) raising the effective free-fall time (t_{ff}) via rotational support (Sormani & Sobacchi 2019). This later paper argues cooling from the hot CGM within $\sim 30^\circ$ of the disc promotes the formation of high-velocity cloud structures. Sormani et al. (2018) models predict hotter gas in the polar di-

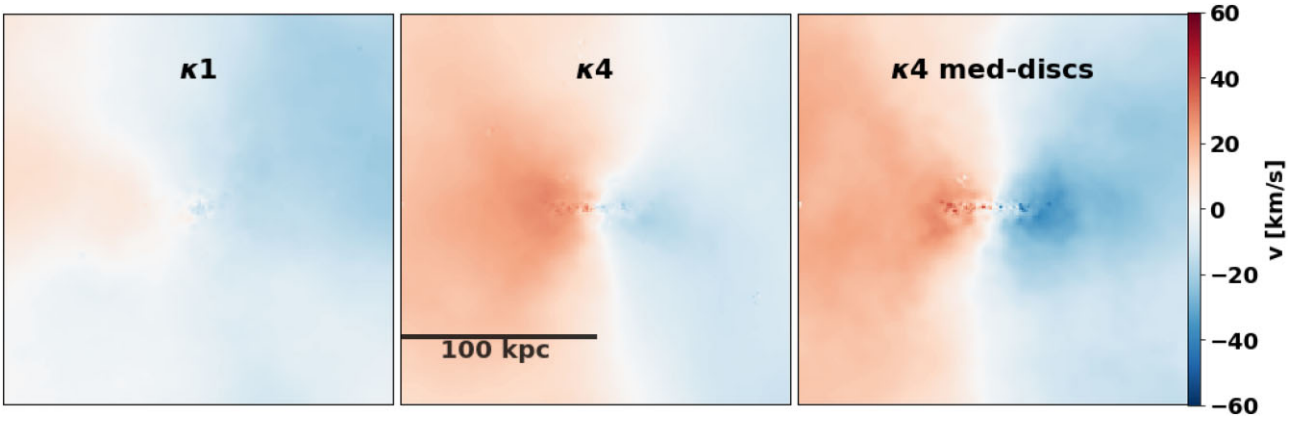

Figure 12. Projected line-of-sight velocity of gas with $T > 10^{5.3}$ K for the $\kappa 1$, $\kappa 4$, and $\kappa 4$-med-discs samples, which are rotated to have their velocities aligned. The med-discs sample has the highest hot gas rotation aligned with the stellar disc. The low level of preferred rotation in the $\kappa 1$ sample probably arises because these galaxies were also rotated based on their stellar velocities.

rection without the presence of outflows, which we do not see in Fig. 10.

Observations of inclined galaxies, including NGC 891, NGC 4631, NGC 5775, and NGC 5907, show enhanced emission along the disc axis, but on the scale of the optical extent of the galaxy within 10 kpc of the centre (Li et al. 2008; Hodges-Kluck et al. 2018, 2020). None of these observations are able to detect significant emission beyond 10 kpc in the equatorial direction, which may be a result of their lower halo masses than our more massive halo stack here. Li & Wang (2013) observed 53 inclined nearby galaxies, although they do not quantify equatorial to polar X-ray morphology. Juráňová et al. (2020) observed six lenticular, S0 galaxies finding enhanced equatorial emission in these galaxies, but mostly within their optical extents. These lenticular galaxies may correspond to our $\kappa 2$ or even $\kappa 3$ galaxies, and live in halo masses at the upper range or above our simulated galaxy halo sample. In all these cases, the X-ray emission is more associated with the hot ISM or disc–halo interface, rather than the CGM.

One may expect polar emission from outflows, especially given that EAGLE launches thermal winds associated with star formation with $T \sim 10^{7.5}$ K (Mitchell et al. 2020). Observationally, there exists extended polar emission associated with starbursts (Strickland et al. 2002, 2004; Strickland & Heckman 2009; Hodges-Kluck et al. 2020), and even moderately star-forming galaxies (Hodges-Kluck et al. 2018). However, it may well be that much of this gas expected to reside at $\sim 10^7$ K is too tenuous to be X-ray bright, therefore the bulk of the mass in the outflow remains undetected (Strickland & Stevens 2000). Outflows along the polar direction are not detected in EAGLE in Mg II absorption either (Ho et al. 2020), and appear to be detected in observations (Bordoloi et al. 2011; Bouché et al. 2012; Lan et al. 2014; Lan & Mo 2018; Huang et al. 2021), which suggests that EAGLE superwind feedback may not reproduce significant aspects of observed outflows.

4.3 Are EAGLE galactic X-ray CGMs too bright?

The EAGLE simulations were not calibrated to reproduce the X-ray luminosities and/or gas fractions in the group and cluster regimes (Crain et al. 2015), which Schaye et al. (2015) demonstrated produced X-ray emission that is too luminous.

It remains less clear if CGM X-ray emission at $M_{200} \lesssim 10^{13}\,\mathrm{M}_\odot$ is also too luminous. As Davies et al. (2019) and Kelly et al. (2021) showed, the Anderson et al. (2015) *ROSAT* stacking could not necessarily rule out EAGLE X-ray luminosities. The best constraints for extended X-ray emission around disc galaxies are from individual targeted galaxies with *Chandra* and *XMM-Newton*, with the latter having the soft X-ray response more closely matching *eROSITA*.

Only the most massive spiral galaxies, NGC 1961 (Anderson et al. 2016), NGC 6753 (Bogdán et al. 2017), NGC 3221 (Das et al. 2019), and the CGM-MASS sample (Li et al. 2017) have detectable extended X-ray emission, which O20 argued are weaker than their high-sSFR *eROSITA* mock stacks containing similar mass galaxies. This potential mismatch is not exclusive to EAGLE, as O20 found similar values $L_{X,>10\mathrm{kpc}}$ in IllustrisTNG, which was also explored by Truong et al. (2020) who concentrates on centralized soft X-ray emission from IllustrisTNG galaxies. The lack of extended emission in deep NGC 891 *XMM-Newton* observations (Hodges-Kluck et al. 2018) may already set an upper limit for detectable emission, which may also suggest that X-ray emission around discs is in reality fainter than EAGLE predicts. It is likely, however, that NGC 891 lives in a halo at the low-mass end of the $\kappa 4$ stack based on its stellar mass.

eROSITA will provide a uniform survey in which to stack many edge-on galaxies, including those at larger distances than our idealized sample at 22 Mpc that are perfectly edge-on. In reality, *eROSITA* will enable the stacking of galaxies at a variety of distances with high-inclination angles, which should work for our proposed experiment to test the presence of ellipsoidal hot gaseous haloes.

4.4 Comparison with Truong et al. (2021)

In a publication addressing similar topics, Truong et al. (2021, hereafter T21) presented physical properties and X-ray predictions of galaxies oriented to be edge-on, focusing on results from the IllustrisTNG (110 Mpc)^3 volume, and additional results from EAGLE. This paper is similar in approach to our work here, but their emphasis is on the extended hot CGM between 0.25 and 0.75 R_{200}. In fact, they find up to a factor 2× stronger emission along the polar axis of both IllustrisTNG and EAGLE, but at $0.5R_{200}$ around $M_{200} = 10^{12.0-12.5}\,\mathrm{M}_\odot$ haloes. While it may seem this contradicts our finding, our focus centres on equatorial enhancement at much smaller radii (10–30 versus 100–150 kpc) and at somewhat higher halo masses ($10^{12.3-12.7}$ versus $10^{12.0-12.5}\,\mathrm{M}_\odot$) in the $\kappa 4$ sample. In fact, T21 finds very slightly enhanced equatorial emission at $0.5R_{200}$

in EAGLE in their fig. 7 for our halo mass range, even though they do not divide their samples by morphology.

Nonetheless, T21 shows similar trends in the physical properties in both IllustrisTNG and EAGLE as we show in Figs 9 and 10, including increased density along the equatorial axis, and increased metallicity and temperature along the polar axis. We do note that the anisotropies in EAGLE are weaker than in IllustrisTNG based on their figs 6 and A2. They also divide their emission maps into bands, finding harder emission along the polar extent, which our proposed experiment would not have the signal to observe. T21 emphasized how different X-ray signatures from IllustrisTNG, EAGLE, and even Illustris (Vogelsberger et al. 2014) could help ascertain the nature of SMBH feedback. For example, Pillepich et al. (2021) demonstrated polar signature associated with feedback events in the higher resolution IllustrisTNG50 volume, and argued that the *eROSITA* bubbles observed above and below the Milky Way disc (Predehl et al. 2020) may be common around other disc galaxies and indicative of episodic jet-driven AGN events.

We note that the T21 predictions of polar-enhanced emission are at lower masses and larger radii, corresponding to SB limits far below what our proposed experiment can detect, $\lesssim 10^{34}$ erg s^{-1} kpc^{-2} (see T21 maps in their fig. 7). Hence, their is a different experiment stacking $\sim 10^4$ galaxies out to $z \sim 0.1$, and based on this work and O20, it may be hard to achieve this detection threshold with standard stacking techniques. It may well be that our proposed experiment detects equatorial enhancement at lower CGM radii, while the T21 polar enhancement exists at larger radii.

5 SUMMARY

We apply an X-ray emission forward modelling pipeline to EAGLE galaxy haloes sorted by stellar morphology to determine how X-ray haloes depend on morphology and to assess the feasibility of detecting azimuthal dependence around edge-on spirals. By stacking mock *eROSITA* observations of gaseous haloes hosting $M_\star = 10^{10.7\text{–}11.2}$ M$_\odot$ galaxies, we predict the following:

(i) Stacked spheroids have more extended and brighter CGMs than disc galaxies. This owes to spheroids living in more massive haloes than discs for our fixed $M_\star$ bin. Related, spheroids have higher average $M_\star$ within this $\Delta \log M_\star = 0.5$ bin, but spheroids are not generally brighter than discs at the exact same $M_\star$. On the other hand, disc galaxies with more overall star formation have brighter emission from their inner 20 kpc. (Figs 2, 3, and 11)

(ii) Edge-on disc galaxies show clear azimuthal dependence with the semimajor axis being up to $60-100$ per cent brighter at 15 kpc than the semiminor axis. Even though thermally driven outflows preferentially travel perpendicular to the disc in EAGLE, this does not translate to higher X-ray emission. The equatorial enhancement of emission appears primarily driven by greater gas densities for $T \gtrsim 10^6$ K gas. (Figs 6, 9, and 10)

(iii) The hotter temperatures of spheroid versus disc CGMs may be observable by taking a ratio at the high and low end of the *eROSITA* soft X-ray response; however, the dependence is weak and may be difficult to detect. (Figs 4 and 5)

(iv) The denser gas along the disc axis relates to net corotation of these hot haloes with the stellar disc. Although these velocities would be difficult to observe directly, we argue that brighter X-ray emission along the semimajor axis correlates with the gas rotation. (Fig. 12)

(v) Our human classification technique to identify edge-on EAGLE disc galaxies creates a cleaner sample in lower-mass haloes to compare to some of the best observed nearby edge-on galaxies, which we predict should have double the emission along the semimajor axis compared to the semiminor axis at 15 kpc. (Fig. 7)

(vi) We note the results by Truong et al. (2021) who find brighter X-ray emission along the semiminor axis mainly at >100 kpc around IllustrisTNG galaxies owing to superwind outflows. We find similar although weaker physical property anisotropies in EAGLE as them, but we argue that this more distant polar gas is too tenuous to measure in our designed experiment.

The detection of the extended hot CGM around inclined galaxies will provide key insights for how galaxies get their gas (e.g. Kereš et al. 2005). While modelling hot gaseous haloes under the assumption of spherical hydrostatic equilibrium may be a good assumption for spheroid-hosting haloes, the deviation from sphericity around disc galaxies (Oppenheimer 2018) can be tested by the axial ratios of hot haloes beyond 10 kpc around discs. Denser, corotating gas along the semimajor axis can better facilitate the cooling of the hot CGM and the condensation of $\sim 10^4$ K phase (Sormani & Sobacchi 2019). Targeting nearby disc galaxy CGMs with *eROSITA* after the completion of the eRASS:8 survey may be worth the investment to ascribe a comprehensive theoretical explanation to multiwavelength observations of the CGM.

ACKNOWLEDGEMENTS

The authors thank the anonymous referee for a thorough review and helpful suggestions. The authors wish to acknowledge Ezra Huscher, Edmund Hodges-Kluck, Joop Schaye, Nhut Truong, and Nastasha Wijers for essential contributions to this work. AN was supported by the University of Colorado Boulder's Undergraduate Research Opportunities Program (UROP), which provides grants to support student-faculty partnerships and projects in all fields of study. BDO, AB, WRF, and RPK acknowledge support from the Smithsonian Institution. RAC is a Royal Society University Research Fellow. AB, RPK, and WRF acknowledge support from the High Resolution Camera program, part of the Chandra X-ray Observatory Center, which is operated by the Smithsonian Astrophysical Observatory for and on behalf of the National Aeronautics Space Administration under contract NAS8-03060. JD is supported by the European Union's Horizon 2020 research and innovation programme under grant agreement no. 818085 GMGalaxies'. This study used high-performance computing facilities at Liverpool John Moores University, partly funded by the Royal Society and LJMU's Faculty of Engineering and Technology.

DATA AVAILABILITY

EAGLE is a publicly available simulation via the data release of McAlpine et al. (2016). X-ray mocks generated from the EAGLE simulation for this work are available to the public upon request by e-mailing benjamin.oppenheimer@colorado.edu.

REFERENCES

Anderson M. E., Bregman J. N., 2011, ApJ, 737, 22
Anderson M. E., Gaspari M., White S. D. M., Wang W., Dai X., 2015, MNRAS, 449, 3806
Anderson M. E., Churazov E., Bregman J. N., 2016, MNRAS, 455, 227
Asplund M., Grevesse N., Sauval A. J., Scott P., 2009, ARA&A, 47, 481
Beckett A., Morris S. L., Fumagalli M., Bielby R., Tejos N., Schaye J., Jannuzi B., Cantalupo S., 2021, MNRAS, 506, 2574
Biffi V., Dolag K., Böhringer H., Lemson G., 2012, MNRAS, 420, 3545

Biffi V., Dolag K., Böhringer H., 2013, MNRAS, 428, 1395
Bogdán Á. et al., 2013a, ApJ, 772, 97
Bogdán Á., Gilfanov M., 2008, MNRAS, 388, 56
Bogdán Á., Forman W. R., Kraft R. P., Jones C., 2013b, ApJ, 772, 98
Bogdán Á., Bourdin H., Forman W. R., Kraft R. P., Vogelsberger M., Hernquist L., Springel V., 2017, ApJ, 850, 98
Booth C. M., Schaye J., 2009, MNRAS, 398, 53
Bordoloi R. et al., 2011, ApJ, 743, 10
Bouché N., Hohensee W., Vargas R., Kacprzak G. G., Martin C. L., Cooke J., Churchill C. W., 2012, MNRAS, 426, 801
Chadayammuri U., Bogdan A., Oppenheimer B., Kraft R., Forman W., Jones C., 2022, ApJL, 936, L15
Comparat J. et al., 2022, preprint (arXiv:2201.05169)
Correa C. A., Schaye J., 2020, MNRAS, 499, 3578
Crain R. A. et al., 2015, MNRAS, 450, 1937
Crain R. A., McCarthy I. G., Frenk C. S., Theuns T., Schaye J., 2010, MNRAS, 407, 1403
Crain R. A., McCarthy I. G., Schaye J., Theuns T., Frenk C. S., 2013, MNRAS, 432, 3005
Dai X., Anderson M. E., Bregman J. N., Miller J. M., 2012, ApJ, 755, 107
Dalla Vecchia C., Schaye J., 2012, MNRAS, 426, 140
Das S., Mathur S., Gupta A., Nicastro F., Krongold Y., Null C., 2019, ApJ, 885, 108
Dauser T. et al., 2019, A&A, 630, A66
Davies J. J., Crain R. A., McCarthy I. G., Oppenheimer B. D., Schaye J., Schaller M., McAlpine S., 2019, MNRAS, 485, 3783
Davies J. J., Crain R. A., Oppenheimer B. D., Schaye J., 2020, MNRAS, 491, 4462
Dolag K., Borgani S., Murante G., Springel V., 2009, MNRAS, 399, 497
Fruscione A. et al., 2006, in Silva D. R., Doxsey R. E., eds, Society of Photo-Optical Instrumentation Engineers (SPIE) Conference Series. p. 62701
Ho S. H., Martin C. L., Kacprzak G. G., Churchill C. W., 2017, ApJ, 835, 267
Ho S. H., Martin C. L., Schaye J., 2020, ApJ, 904, 76
Hodges-Kluck E. J., Bregman J. N., 2013, ApJ, 762, 12
Hodges-Kluck E. J., Miller M. J., Bregman J. N., 2016, ApJ, 822, 21
Hodges-Kluck E. J., Bregman J. N., Li J.-T., 2018, ApJ, 866, 126
Hodges-Kluck E. J., Yukita M., Tanner R., Ptak A. F., Bregman J. N., Li J.-T., 2020, ApJ, 903, 35
Hopkins P. F., 2013, MNRAS, 428, 2840
Huang Y.-H., Chen H.-W., Shectman S. A., Johnson S. D., Zahedy F. S., Helsby J. E., Gauthier J.-R., Thompson I. B., 2021, MNRAS, 502, 4743
Juráňová A. et al., 2020, MNRAS, 499, 5163
Kacprzak G. G. et al., 2019a, ApJ, 870, 137
Kacprzak G. G. et al., 2019b, ApJ, 870, 137
Kacprzak G. G., Churchill C. W., Nielsen N. M., 2012, ApJ, 760, L7
Kacprzak G. G., Muzahid S., Churchill C. W., Nielsen N. M., Charlton J. C., 2015, ApJ, 815, 22
Kelly A. J., Jenkins A., Frenk C. S., 2021, MNRAS, 502, 2934
Kereš D., Katz N., Weinberg D. H., Davé R., 2005, MNRAS, 363, 2
Lan T.-W., Mo H., 2018, ApJ, 866, 36
Lan T.-W., Ménard B., Zhu G., 2014, ApJ, 795, 31
Li J.-T., Wang Q. D., 2013, MNRAS, 428, 2085
Li J.-T., Li Z., Wang Q. D., Irwin J. A., Rossa J., 2008, MNRAS, 390, 59
Li J.-T., Bregman J. N., Wang Q. D., Crain R. A., Anderson M. E., Zhang S., 2017, ApJS, 233, 20
Martin C. L., Ho S. H., Kacprzak G. G., Churchill C. W., 2019, ApJ, 878, 84
McAlpine S. et al., 2016, Astron. Comput., 15, 72
Merloni A. et al., 2012, preprint (arXiv:1209.3114)
Mitchell P. D., Schaye J., Bower R. G., Crain R. A., 2020, MNRAS, 494, 3971
Nelson D. et al., 2018, MNRAS, 475, 624
Oppenheimer B. D. et al., 2020, ApJ, 893, L24 (O20)
Oppenheimer B. D., 2018, MNRAS, 480, 2963
Péroux C., Nelson D., van de Voort F., Pillepich A., Marinacci F., Vogelsberger M., Hernquist L., 2020, MNRAS, 499, 2462
Pillepich A. et al., 2018a, MNRAS, 473, 4077
Pillepich A., Reiprich T. H., Porciani C., Borm K., Merloni A., 2018b, MNRAS, 481, 613
Pillepich A., Nelson D., Truong N., Weinberger R., Martin-Navarro I., Springel V., Faber S. M., Hernquist L., 2021, MNRAS, 508, 4667
Planck Collaboration XI, 2013, A&A, 557, A52
Predehl P. et al., 2020, Nature, 588, 227
Predehl P. et al., 2021, A&A, 647, A1
Rasmussen J., Sommer-Larsen J., Pedersen K., Toft S., Benson A., Bower R. G., Grove L. F., 2009, ApJ, 697, 79
Rosas-Guevara Y. M. et al., 2015, MNRAS, 454, 1038
Schaller M., Dalla Vecchia C., Schaye J., Bower R. G., Theuns T., Crain R. A., Furlong M., McCarthy I. G., 2015, MNRAS, 454, 2277
Schaye J. et al., 2015, MNRAS, 446, 521
Schaye J., Dalla Vecchia C., 2008, MNRAS, 383, 1210
Sharma P., McCourt M., Quataert E., Parrish I. J., 2012, MNRAS, 420, 3174
Shen S., Madau P., Guedes J., Mayer L., Prochaska J. X., Wadsley J., 2013, ApJ, 765, 89
Smith R. K., Brickhouse N. S., Liedahl D. A., Raymond J. C., 2001, ApJ, 556, L91
Sormani M. C., Sobacchi E., 2019, MNRAS, 486, 215
Sormani M. C., Sobacchi E., Pezzulli G., Binney J., Klessen R. S., 2018, MNRAS, 481, 3370
Springel V., 2005, MNRAS, 364, 1105
Springel V., White S. D. M., Tormen G., Kauffmann G., 2001, MNRAS, 328, 726
Stewart K. R. et al., 2017, ApJ, 843, 47
Strickland D. K., Heckman T. M., 2009, ApJ, 697, 2030
Strickland D. K., Stevens I. R., 2000, MNRAS, 314, 511
Strickland D. K., Heckman T. M., Weaver K. A., Hoopes C. G., Dahlem M., 2002, ApJ, 568, 689
Strickland D. K., Heckman T. M., Colbert E. J. M., Hoopes C. G., Weaver K. A., 2004, ApJS, 151, 193
Thob A. C. R. et al., 2019, MNRAS, 485, 972
Toft S., Rasmussen J., Sommer-Larsen J., Pedersen K., 2002, MNRAS, 335, 799
Trapp C. W. et al., 2022, MNRAS, 509, 4149
Truong N. et al., 2020, MNRAS, 494, 549
Truong N., Pillepich A., Nelson D., Werner N., Hernquist L., 2021, MNRAS, 508, 1563 (T21)
Vogelsberger M. et al., 2014, MNRAS, 444, 1518
Wiersma R. P. C., Schaye J., Smith B. D., 2009a, MNRAS, 393, 99
Wiersma R. P. C., Schaye J., Theuns T., Dalla Vecchia C., Tornatore L., 2009b, MNRAS, 399, 574
ZuHone J. A., Hallman E. J., 2016, Astrophysics Source Code Library, record ascl:1608.002

This paper has been typeset from a TEX/LATEX file prepared by the author.